Supporting Information

Scalable Nanoarchitectonics with Microporous Polymer Composite for Methanol-Tolerant ORR Electrocatalysts

Abin Sebastian, Atanu Panda, Ravi Nandan, Joel Henzie, Ovidiu Cretu, Jian Xu, Nadiia Velychkivska, Renzhi Ma, Pooja Gakhad, Abhishek Kumar Singh, Gary J. Richards, Koji Kimoto, Lok Kumar Shrestha, Katsuhiko Ariga, Yusuke Yamauchi, Jonathan P Hill*

Contents

1.0 General Experimental. Morphology of the materials was investigated by using field emission scanning electron microscopy (FE-SEM). Samples were mounted on silicon wafer prior to coating by Pt sputtering using a Hitachi E-1030 Ion Sputterer. Observations were made using a Hitachi SU8000 FE-SEM operating at an accelerating voltage of 5 keV. TEM characterization was performed using a ThermoFisher Scientific Titan microscope equipped with a probe aberration corrector. The microscope was operated in scanning (STEM) mode at an acceleration voltage of 300 kV and a probe current of ~30 pA. Images were collected using a high-angle annular dark-field (HAADF) detector. HR-TEM measurements were made on samples deposited by dropping of a diluted colloidal suspension in ethanol onto a TEM grid. Images were collected at an accelerating voltage of 200 kV using a JEOL 2100F field emission transmission electron microscope. X-ray diffraction (XRD) characterization was performed on a BRUKER D2 PHASER equipped with a copper X-ray tube and a LynxEye linear detector. FT-IR spectroscopy was performed on Nicolet, Model Nexus 670 instrument in the wavenumber range of 4000-400 cm^{-1}. Raman spectroscopy was performed using a microscope confocal Raman spectrometer, JASCO NRS-3100. Surface elemental analyses of the samples was performed using X-ray photoelectron spectroscopy (XPS) using a PHI Quantera SXM system. The samples for XPS measurement were deposited on carbon tape and mounted on the holder. The MultiPak software was used to process all XPS data. All spectra were corrected against the C1s signal (284.6 eV) and fitted. Nitrogen adsorption-desorption analysis was conducted using an Autosorb iQ (Quantachrome, Inc.) at 77 K. Specific surface areas were evaluated using the Brunauer-Emmett-Teller method. Samples were degassed at 120 °C for 6 h under vacuum before nitrogen physisorption measurements. X-ray absorption fine structure spectra (Co Kedge) were collected at BL-12C beamline in Photon Factory, Japan (KEK-PF). The Co K-edge spectra of all the samples were recorded under fluorescence excitation mode using a Lytle detector. The XAS data were analyzed using Athena and Artemis software.

Porous Porphyrin Polymer (**PPP**).[S1] Anhydrous aluminum chloride (4.4 g, 22 mmol) was added to a solution containing *meso*-5,10,15,20-tetraphenylporphyrin[S2] (1 g, 1.6 mmol) in refluxing dichloromethane (30 mL). The mixture was then stirred at reflux for 24 h under a nitrogen atmosphere. The reaction mixture was allowed to cool to room temperature, the resulting black precipitate collected by filtration, and washed with water (CAREFUL! Anhydrous $AlCl_3$ reacts vigorously with water) and ethanol. The resulting solid was then treated consecutively with ethanol, chloroform, tetrahydrofuran, acetone, and methanol by refluxing with each solvent for six hours. After each reflux procedure, the solid was filtered and suspended in the following treatment solvent. The resulting brown product (**PPP**) was ground into a fine powder and dried in a vacuum oven at 80 °C for 18 h. Yield: 104%, N_2 adsorption (77K): SA_{BET} : 1178 m^2/g, Pore Volume 1.1 cc/g. FTIR: $\nu_{benzene}$ 1450-1640cm^{-1}, $\nu_{C\text{-}H\ Benzene\ out\ of\ plane}$:1250-1180cm^{-1}, $\nu_{benzeneC\text{-}H\text{-}\ in\ plane}$ 1070-650cm^{-1}

Metalation of PPP (PPP-Co). Post-metalation was carried out by direct metalation of **PPP**. **PPP** (200 mg) was dispersed in *N*,*N*-dimethylformamide (DMF) and heated to reflux. Cobalt chloride hexahydrate (200 mg) was then carefully added and reflux continued for 18 h. The reaction mixture was allowed to cool to room temperature, the solid precipitate was filtered and washed several times with ethanol then dried in a vacuum oven at 80 °C for 18 h. The resulting **PPP-Co** was characterized using FTIR, XPS, SEM, and TEM. Yield: 95.6%, Co content (XPS) : 0.8at%, N_2 Adsorption (77K): SA_{BET} : 969 m^2/g, Pore Volume : 0.856 cc/g, FTIR: $\nu_{N\text{-}Co}$ 1004 cm^{-1}

Co-NP/Co-SA@NPC, **Co-SA@NPC** and **Co-NP@NPC**. **Co-NP/Co-SA@NPC** was prepared by thermolyzing **PPP-Co** (200 mg) loaded in an alumina crucible in a tube furnace. The temperature of the tube furnace fitted with inert gas flow was increased to 1000 degree at a rate of 5 °C min^{-1} then maintained at that temperature for 2 h followed by cooling under inert

gas flow under ambient conditions, yielding **Co-NP/Co-SA@NPC**. **Co-NP/Co-SA@NPC** was etched to remove cobalt nanoparticles by treating with concentrated hydrochloric acid (12 M) for 48 h followed by copious washing with milli-Q water then ethanol, to obtain **Co-SA@NPC.** For the preparation of **Co-NP@NPC**, **PPP** (200 mg) was treated with cobalt chloride hexahydrate (200 mg) in methanol-water mixture (1:1, 15 mL) at 125 °C for 8 h. The product obtained was thermolyzed at 1000 degrees under inert conditions. Control samples were also prepared by the thermolysis of **PPP-Co** at different temperatures (500, 700, 900 °C) selected based on thermogravimetric analysis (TGA) data.

Electrochemistry. Electrochemical studies (ORR, impedance, C_{dl}, etc.) were performed using a Biologic VMP3 electrochemical analyzer consisting of a three-electrode system where the electrocatalyst-modified glassy carbon electrode (active geometric areas: for RDE ~0.07 cm^2, RRDE ~0.196 cm^2), KCl saturated Ag/AgCl, and a Pt ring are employed respectively as working, reference, and counter electrodes. For the working electrode, subject catalyst material (7 mg) was dispersed into a mixed solution containing deionized water (0.5 mL), ethanol (0.5 mL), and Nafion® solution (5 wt%, 15 μL) following by ultrasonication of the resulting mixture for 1 h yielding a well-dispersed slurry. The corresponding catalyst loading at the electrode was 0.5 mg cm^{-2}. All electrocatalytic tests were carried out in an oxygen- or nitrogen-saturated 0.1 M KOH solution. Cyclic voltammetry (CV) tests were recorded at a scan rate of 25 mV s^{-1} under static conditions after the system reached a stable state. The linear sweep voltammetry (LSV) ORR polarization plots were recorded at 1600 rpm at a scan rate of 10 mV s^{-1} using a rotating ring electrode (RDE). All electrochemical potentials were measured against Ag/AgCl then converted relative to the reversible hydrogen electrode (RHE) using the equation:

$E_{RHE} = E^{o}_{Ag/AgCl} + (0.059*pH) + E_{Ag/AgCl}$, where $E^{o}_{Ag/AgCl}$ is 0.197 V vs. SHE

Further insight into the ORR process was evaluated through the electron transfer number (n) and hydrogen peroxide formation $\%HO_2^-$ measurements calculated from the RRDE-LSV polarization curve by applying the following equations:

$$n = 4\,x\,\frac{I_d}{I_d + {I_R}/{N}}$$

$$\%HO_2^- = 200\,x\,\frac{{I_R}/{N}}{I_D + {I_R}/{N}}$$

where I_D and I_R represent the disc and ring currents, respectively, and N = 0.3 is the collection efficiency of the Pt ring. For the methanol tolerance test, the electrode was rotated at 1600 rpm for 400 s after injection of methanol into the cell to ensure that the added methanol had been homogeneously dispersed. Durability evaluations were carried out from the i–t chronoamperometric responses of the electrodes in an aqueous solution of KOH (0.1 M) saturated with O_2 rotating at 800 rpm. The double layer capacitance, C_{dl} of the catalytic surface and electrochemically active surface area, ECSA of **PPP-Co/T** were evaluated by CV at non-Faradaic potential ranging from -0.05 to 0.05 V (vs. Ag/AgCl) at different scan rates (10, 20, 40, 60, 80, 100 mV s^{-1}) in a nitrogen-saturated 0.1 M KOH solution. C_{dl} was evaluated from the slope of linear regression of the ΔJ $(J_a - J_c)/2$ at 0 V (vs. Ag/AgCl) against the scan rate. J_a and J_c are the current density of anode and cathode at 0 V (vs. Ag/AgCl).

$$ECSA\ (in\ cm^{-2}) = \frac{C_{dl}}{C_s}$$

$$R_f = \frac{ECSA}{A_g}$$

Computational Methodology. To gain further insights into reaction mechanism, first-principles calculations were performed using density functional theory as implemented in the Vienna Ab-initio Simulation Package (VASP).[S3] All electron projector augmented wave (PAW) pseudopotentials were used to describe electron-ion interactions.[S4] The electron exchange and correlations were approximated using Perdew-Burke-Ernzerhof (PBE) generalized gradient approximation (GGA).[S5] The Atomic Simulation Environment (ASE)[S6] toolkit was used to construct the thirteen Co atom icosahedron nanocluster. To prevent spurious interaction between periodic images, a vacuum of 20 Å was applied along z direction. The Brillouin zone was sampled using Monkhorst pack with 2*2*1 grid for all calculations. Plane wave cut-off of 500 eV was used. All structures were fully relaxed using a conjugate gradient scheme until the convergence criteria for energies and forces reached 10−4 eV and 0.01 eV Å-1, respectively. As PBE does not incorporate the weak dispersion forces, an empirical atom-pairwise correction proposed by Grimme et al[S7] in terms of the DFT-D2 scheme was utilized to describe the long-range van der Waals interactions. The Bader charge scheme, implemented in Henkelman code,[S8] was utilised to study the degree of charge distribution. The extraction of zero-point energy and entropy contribution for vibrational energy calculations was performed using VASPKIT.[S9]

2.0 Supplementary Figures

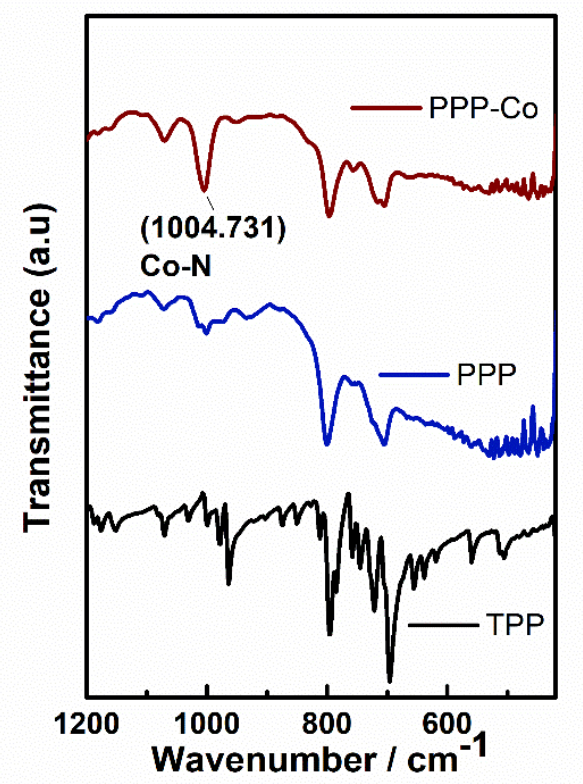

Figure S1. Infrared spectra in the fingerprint region: *meso*-tetraphenylporphyrin (TPP) monomer, TPP porous porphyrin polymer (**PPP**), metalled porphyrin polymer (**PPP-Co**).

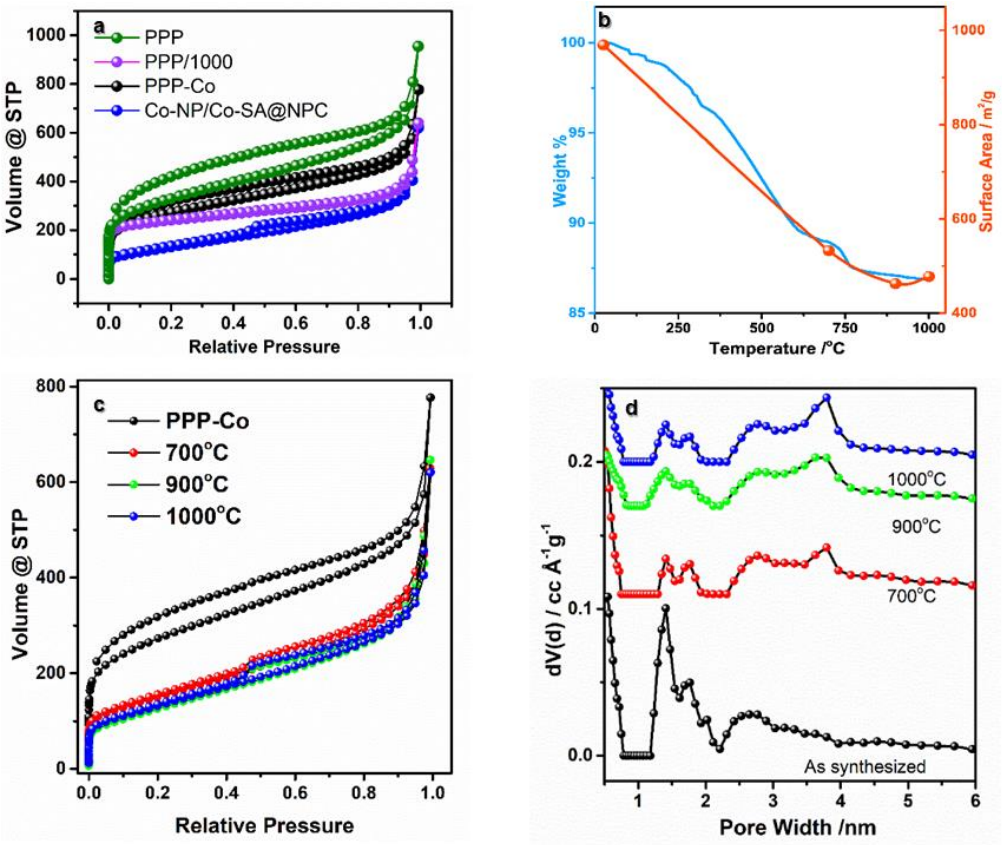

Figure S2. (a) Nitrogen Isotherms (77K) of **PPP**, **PPP/1000**, **PPP-Co** and **Co-NP/Co-SA@NPC** (b) Thermogravimetric analysis with temperature dependence of surface area for **Co-NP/Co-SA@NPC**. (c) Nitrogen Isotherms (77K) and (d) Pore distribution of samples at various pyrolytic temperature.

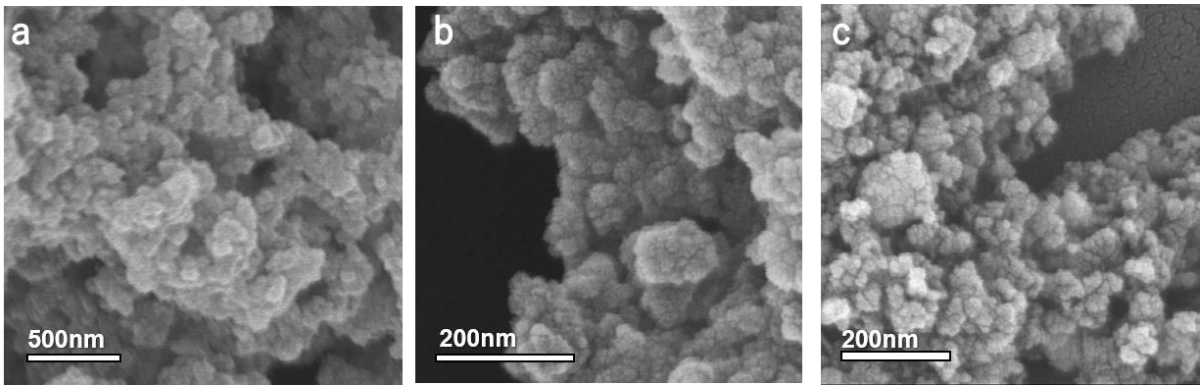

Figure S3. Scanning electron microscopic images of (from left) **PPP, PPP-Co, Co-NP/Co-SA@NPC**.

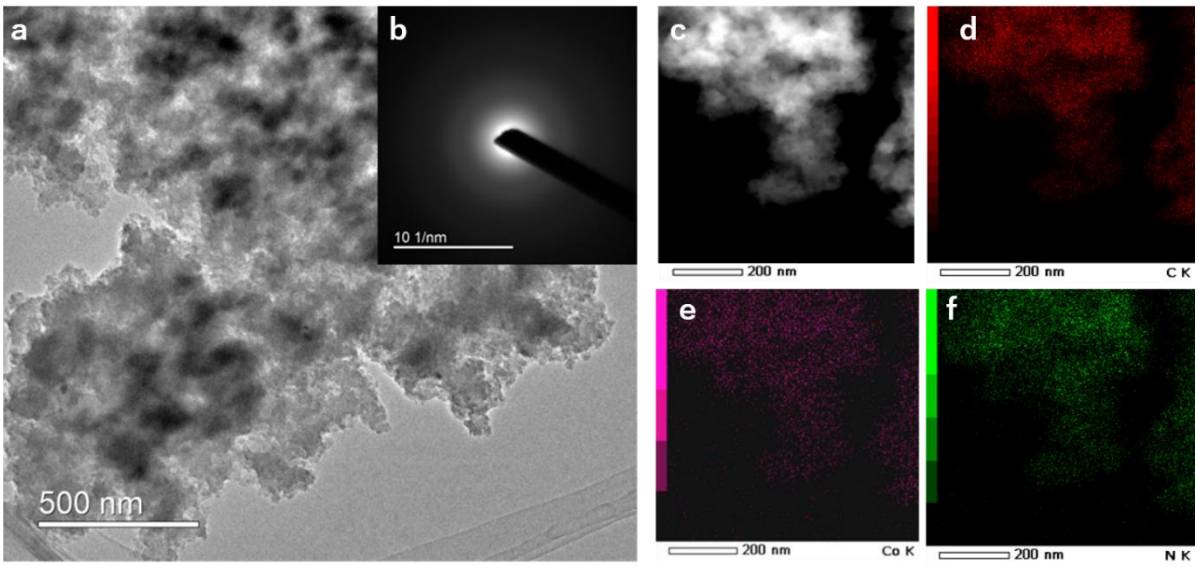

Figure S4. (a) Transmission electron microscopic images of PPP-Co. (b) Selected Area Electron Diffraction (SAED) and (c-f) Energy Dispersive X-ray Spectroscopy (EDX) of PPP-Co showing carbon (red), nitrogen (green), cobalt (purple).

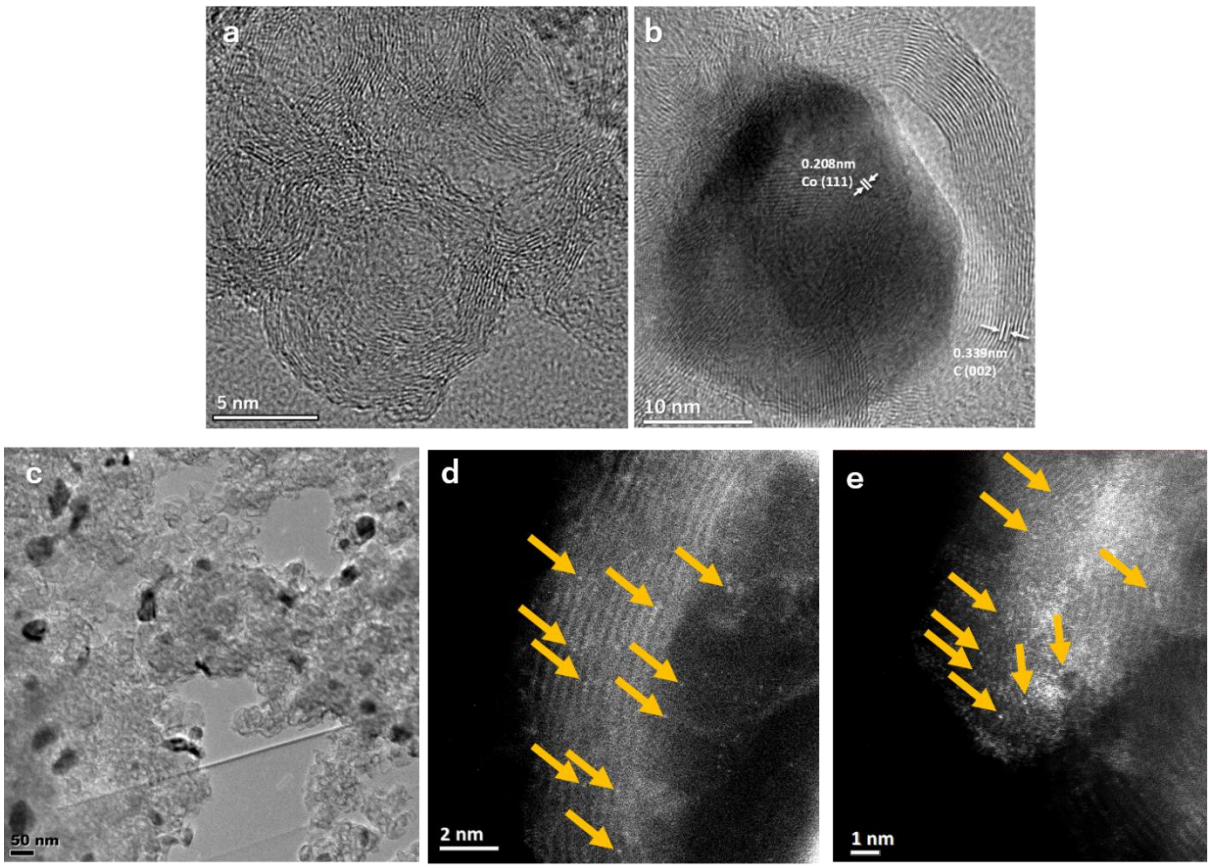

Figure S5. HR-TEM images of (a) **Co-SA@NPC**, (b) **Co-NP@NPC**, (c) **Co-NP/Co-SA@NPC**, (d-e) ac-HAADF STEM of **Co-NP/Co-SA@NPC**.

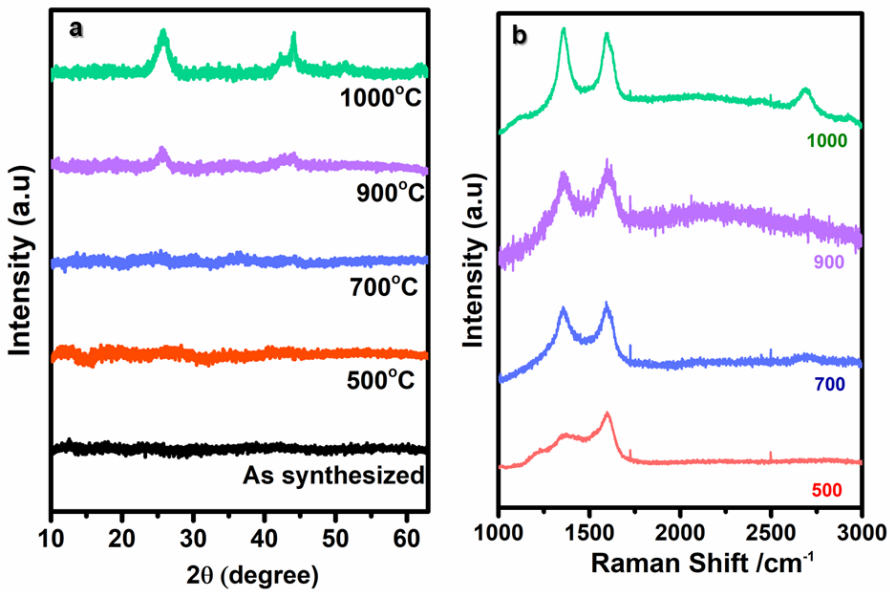

Figure S6. (a) Powder XRD and (b) Raman Spectra of **PPP-Co** and catalyst particles pyrolyzed at various temperatures.

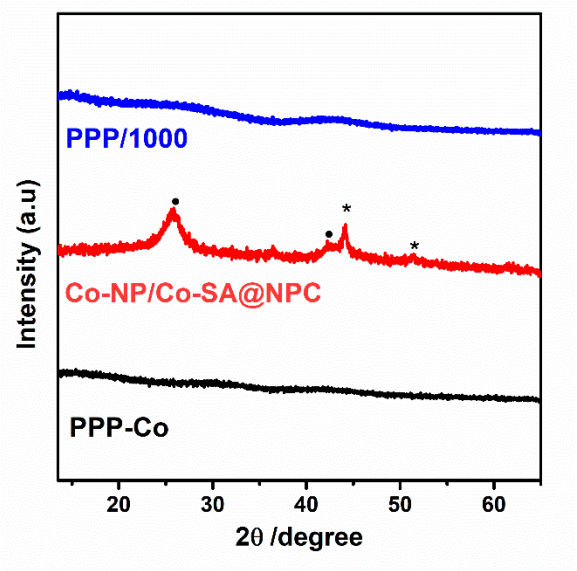

Figure S7. Powder XRD patterns of **PPP-Co**, **PPP/1000**, **Co-NP/Co-SA@NPC**.

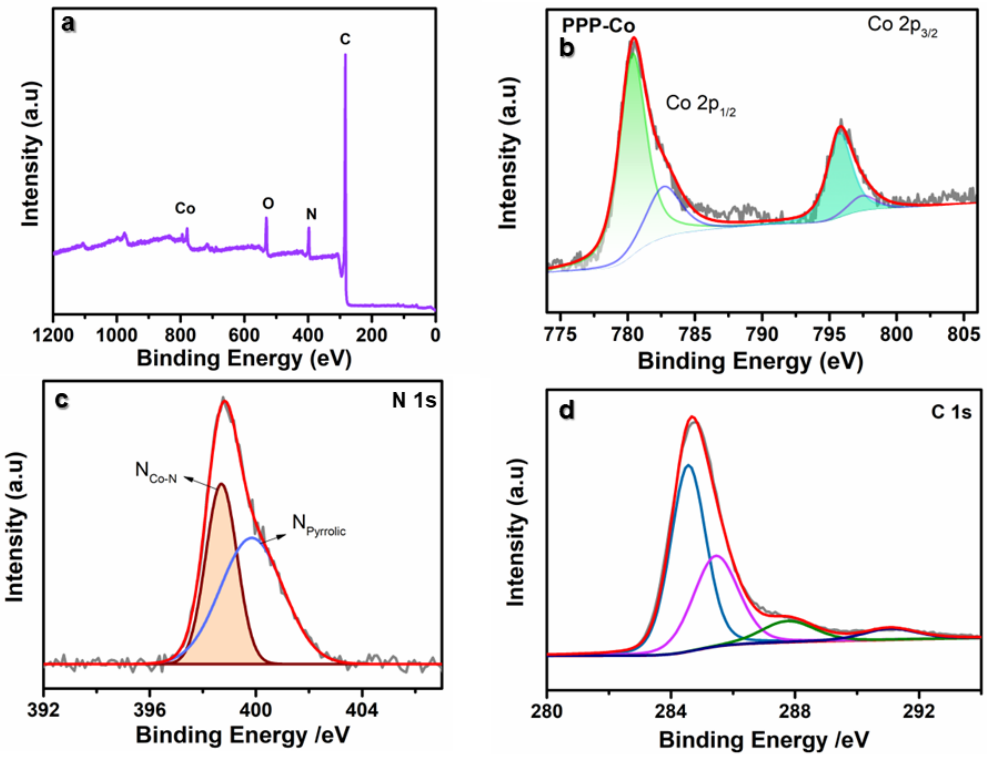

Figure S8. XPS data for **PPP-Co**. (a) XPS survey spectrum. (b) Deconvoluted high resolution Co 2p spectrum. (c) Deconvoluted high resolution N1s spectrum. (d) Deconvoluted high resolution C1s spectrum.

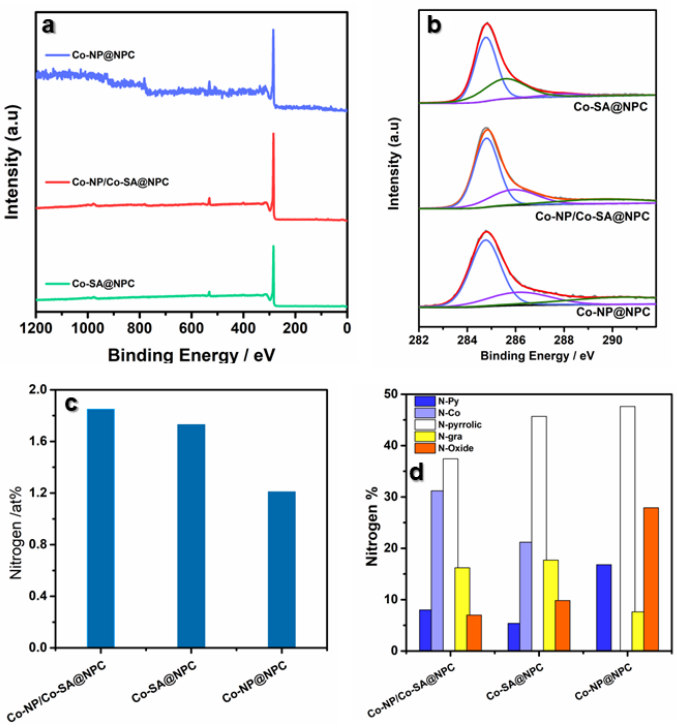

Figure S9. Summary of XPS data for selected materials. (a) XPS Survey Spectra. (a) Deconvoluted high resolution C1s spectrum. (a) Nitrogen contents extracted from XPS spectra. (d) Types of nitrogen in **Co-NP/Co-SA@NPC**, **Co-NP @NPC** and **Co-SA@NPC**

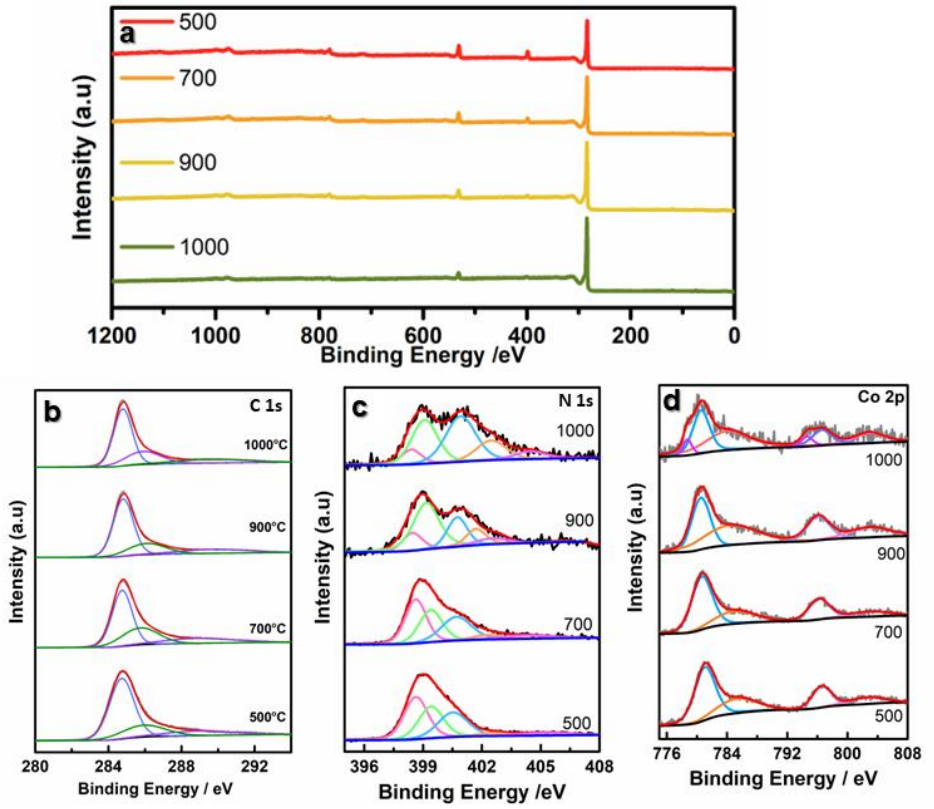

Figure S10. XPS of materials obtained at different thermolysis temperatures. (a) XPS survey spectra. (b) Deconvoluted high resolution C1s XPS spectra. (c) Deconvoluted high resolution N 1s spectra. (d) Deconvoluted high resolution Co2p spectra.

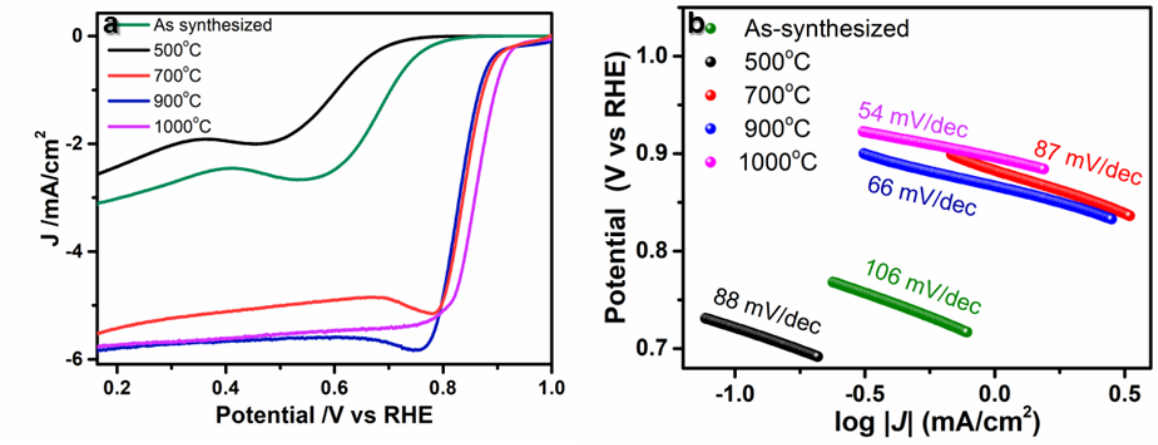

Figure S11. Thermolysis temperature – comparison of electrochemical data. a) LSV polarisation curves and b) Tafel plots.

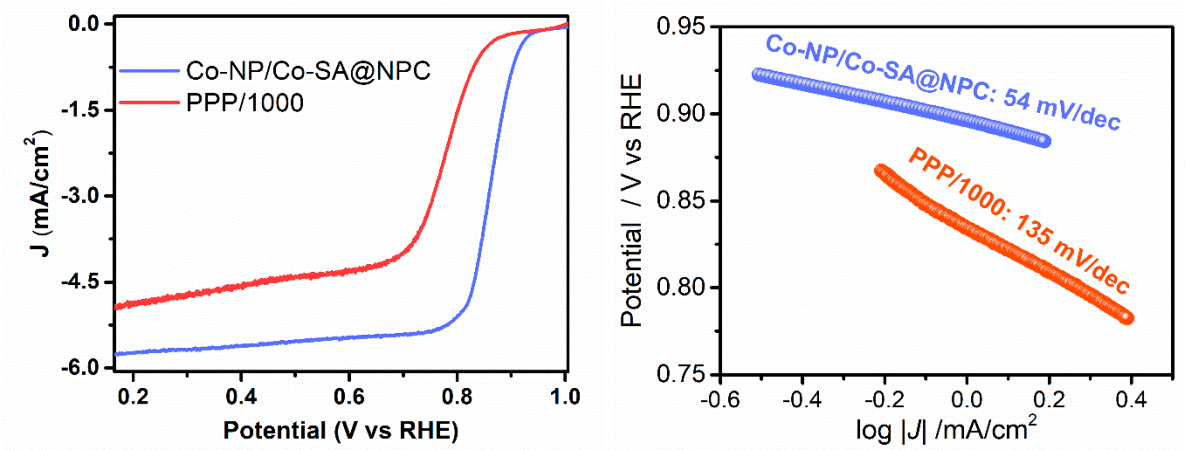

Figure S12. Comparison of electrochemical data for **PPP-1000** and **CoNP/CoSA@NPC** (absence and presence of cobalt, resp.): (Left panel) LSV polarisation curve and (Right panel) Tafel plot of with and without Cobalt

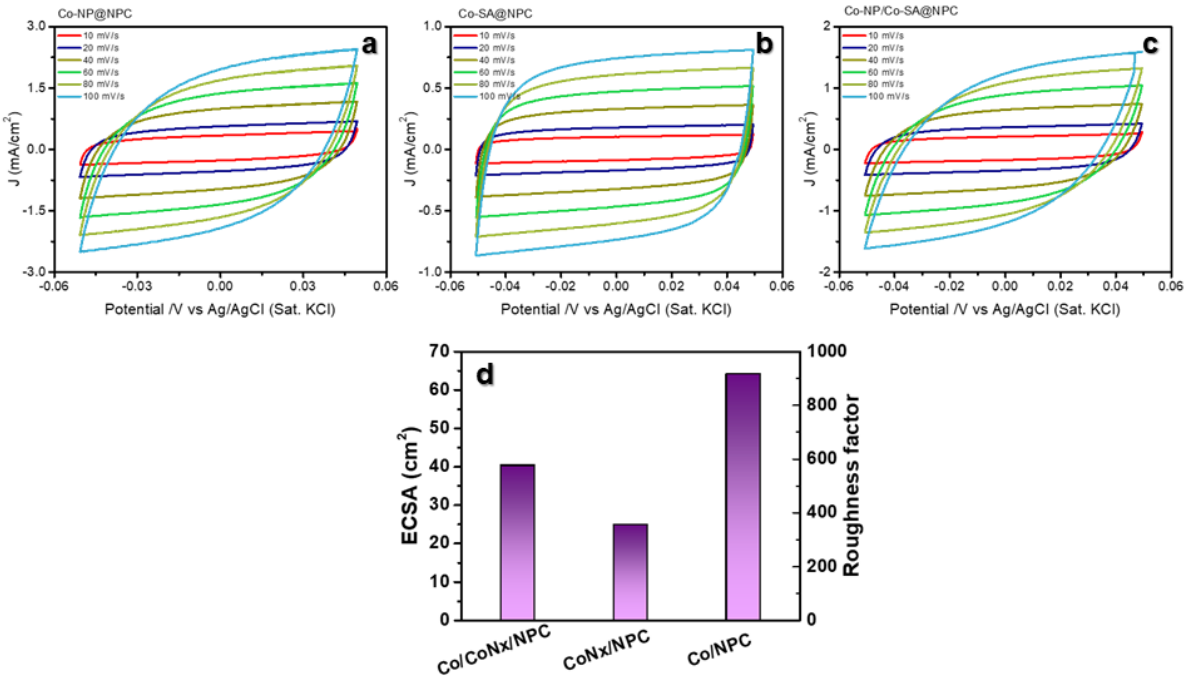

Figure S13. Scan-rate dependent Cyclic Voltammetric measurement for (a) **Co-NP@NPC**, (b) **Co-SA@NPC** and (c) **Co-NP/Co-SA@NPC**. (d) Electrochemical Surface Area (ECSA) and Roughness factor of Catalysts.

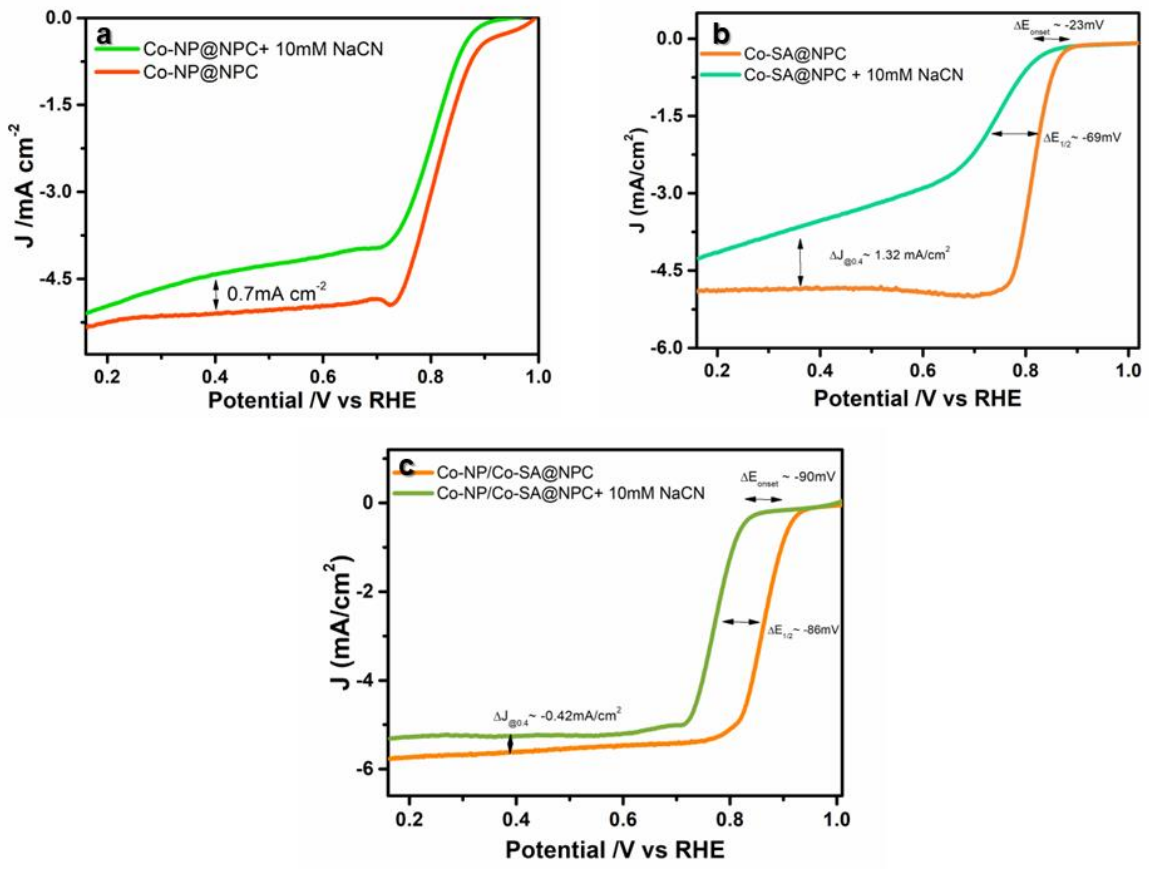

Figure S14. Poisoning (cyanide) studies for (a) **Co-NP@NPC**, (b) **CoSA@NPC**, and (c) **Co-NP/CoSA@NPC**.

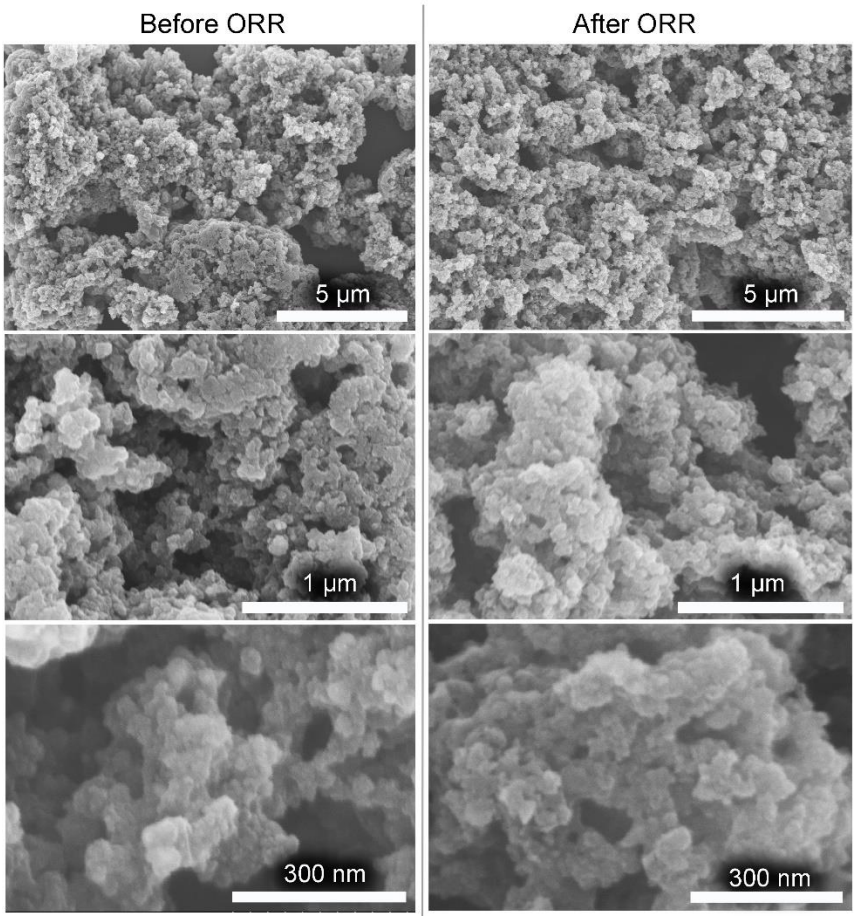

Figure S15. Electrocatalyst durability: SEM images prior to and following ORR (24 h) of **Co-NP/CoSA@NPC**. Note that, for comparative purposes, samples also contain binder according to the details given in the experimental section. Left side: SEM images of **Co-NP/CoSA@NPC** prior to ORR (top to bottom: increasing magnification). Right side: SEM images of the same sample of **Co-NP/CoSA@NPC** following application of ORR (top to bottom: increasing magnification). An amorphous nanoparticulate morphology is observed, and there is essentially no variation in the morphology after ORR process.

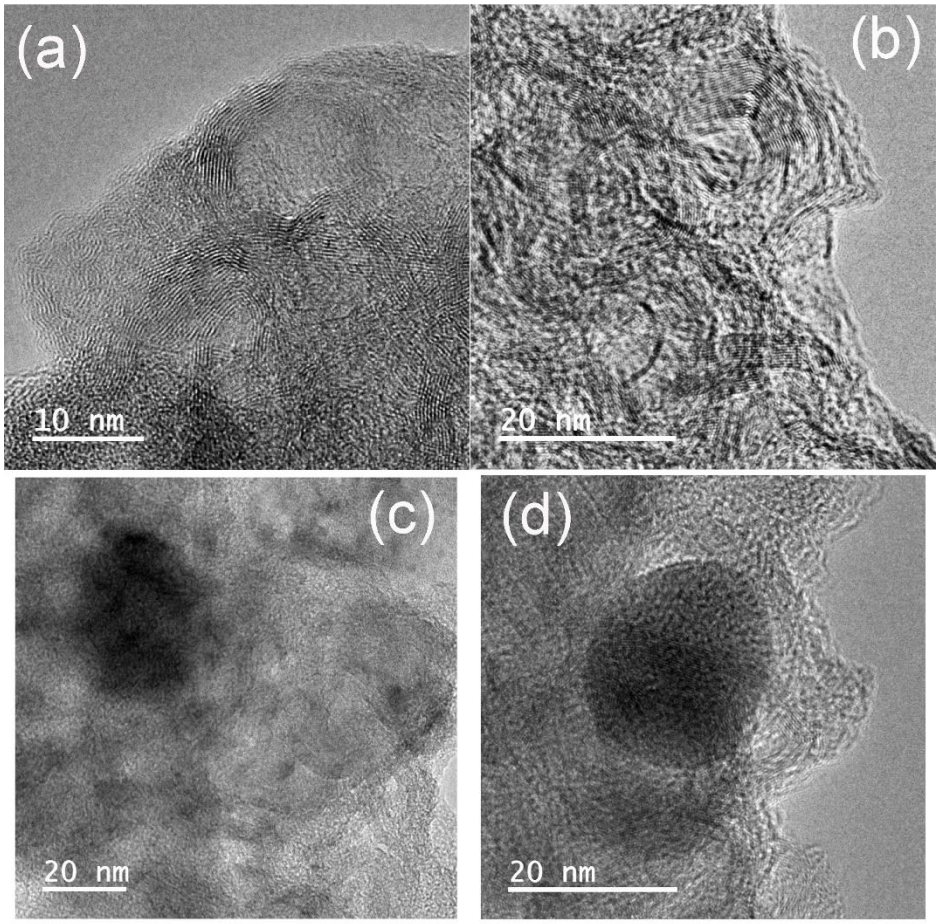

Figure S16. Electrocatalyst durability: HRTEM images (a,c) prior to and (b,d) following ORR (24 h) of **Co-NP/CoSA@NPC**. Panels (a) and (b) show that the pristine graphitic structure is persistent with voids also remaining in the carboniferous structure after ORR. Panels (c) and (d) show that **Co-NP**s also persist following ORR. Graphitic wrapping of **Co-NP** is also apparent in (d).

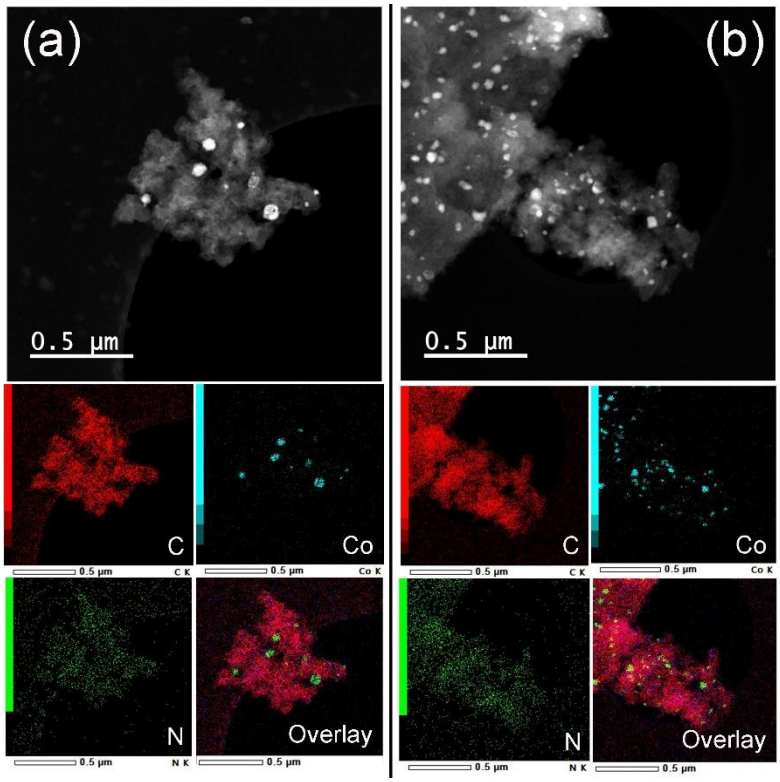

Figure S17. Electrocatalyst durability: (a) Bright field STEM images and corresponding EDX analyses of **Co-NP/CoSA@NPC** prior to ORR. (a) Bright field STEM images and corresponding EDX analyses of **Co-NP/CoSA@NPC** after ORR. Carbon, nitrogen and cobalt content are all maintained following ORR. Overlay EDX images indicate that the components remain integrated in the sample after ORR process.

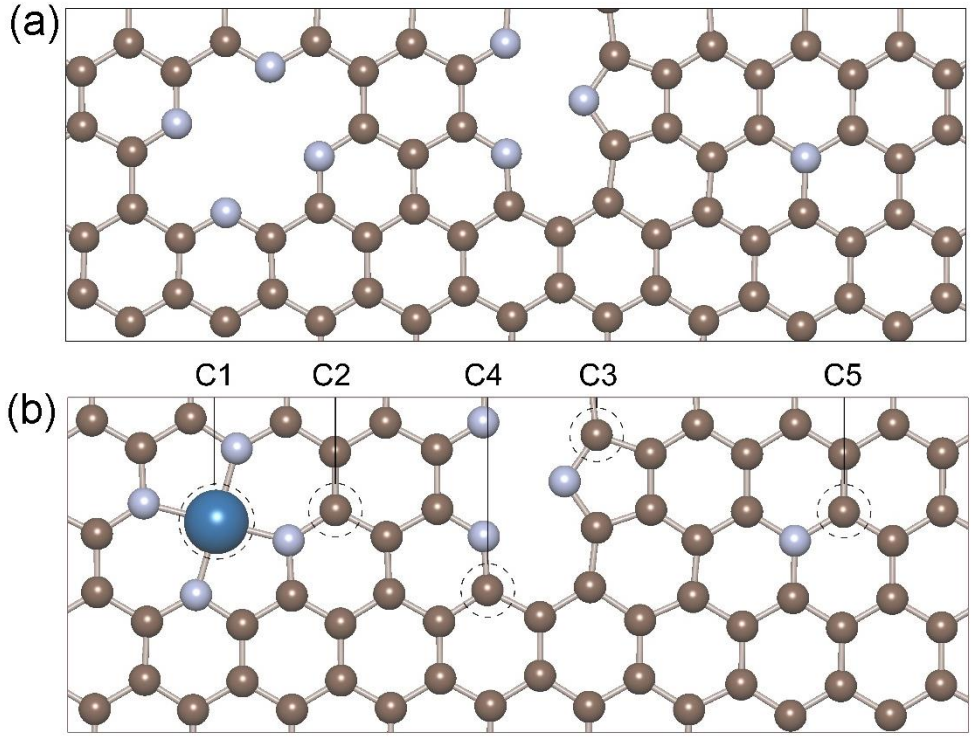

Figure S18. Computed structures. (a) Different N-doping sites in **NPC**. (b) The initially used example of **Co-SA@NPC** with binding sites C1–C5 shown.

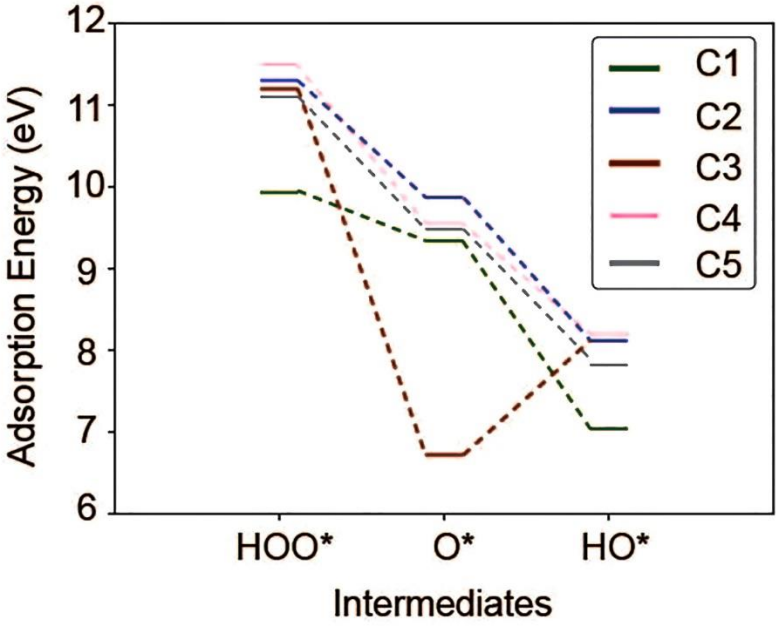

Figure S19. Adsorption energy profile of ORR intermediates adsorbed over five configurations C1, C2, C3, C4 and C5 on **Co-SA@NPC**.

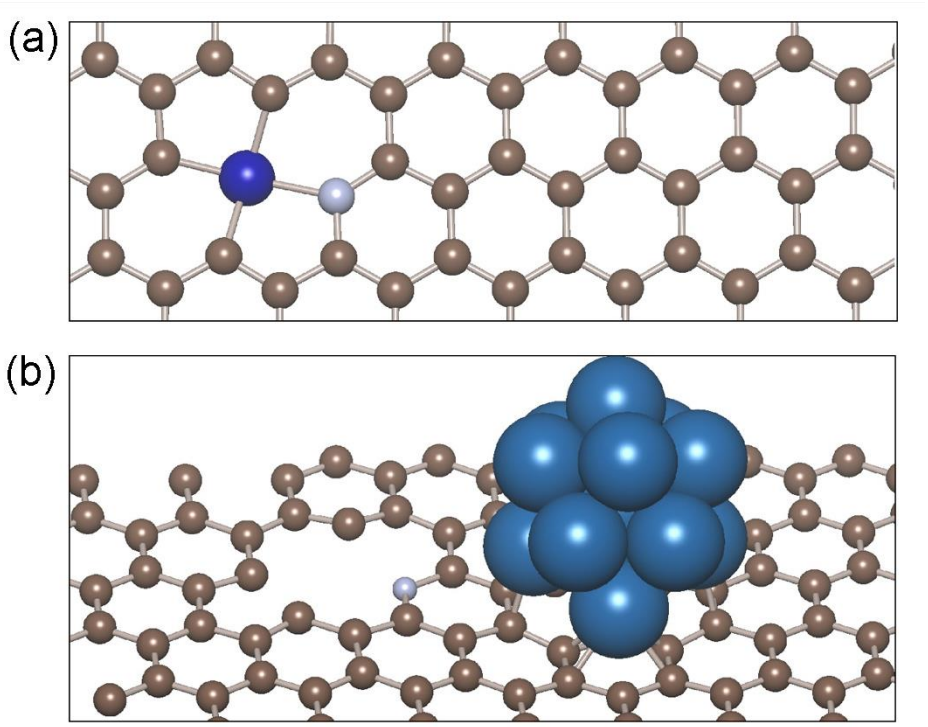

Figure S20. Structures of (a) **Co-SA@NPC** and (b) **Co-NP@NPC** selected for computational scrutiny in ORR processes.

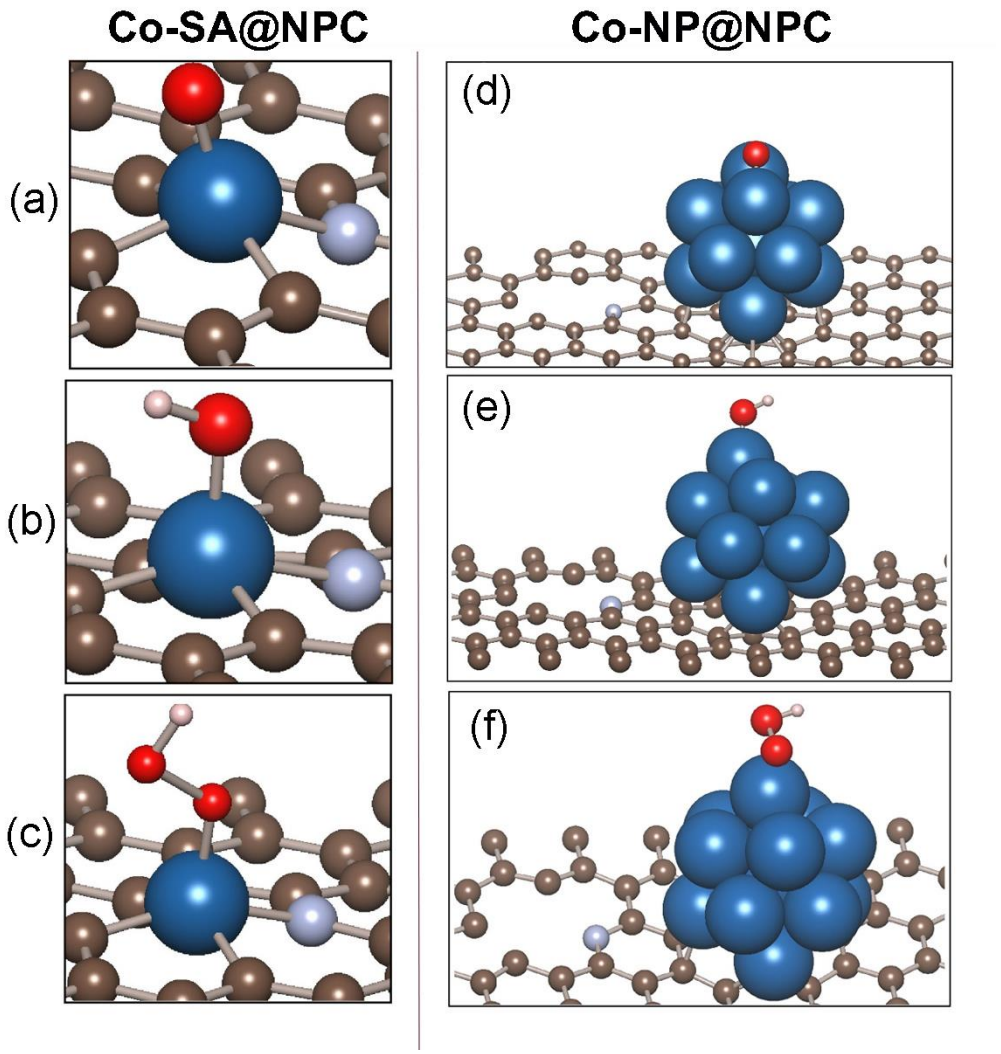

Figure S21. Left side: reactive intermediates bound at cobalt atom in **Co-SA@NPC** (a) O*, (b) HO*, and (c) HOO*. Right side: reactive intermediates bound at cobalt atom in **Co-NP@NPC** (d) O*, (e) HO*, and (f) HOO*.

3.0 Supplementary Tables

Table S1. Electrochemical data from control experiments.

Sample	E_{onset}	$E_{1/2}$	J_{dl}	$J_{k@0.8}$	Tafel slope
Co-NP/Co-SA@NPC	960	865	-5.6	57	54.5
Co-SA@NPC	870	815	-4.8	12	56.6
Co-NP @NPC	910	820	-5.1	7.5	100
Pt/C	1000	860	-5.3	25.7	102

Table S2. Electrochemical experimental data of different thermolysis temperatures.

Sample	E_{onset}	$E_{1/2}$	J_{dl}	Tafel slope
1000 or Co-NP/Co-SA@NPC	960	865	-5.6	54.5
900	925	835	-5.6	66.5
700	920	853	-5.4	86.9
500	736	560	-1.9	88.7

Table S3. Bader charge transfer of O*, HO* and HOO* over **Co-SAC@NPC** and **Co-NP@NPC**

	Co	O1	O2	H	N
HOO*					
Co-SA@NPC	0.89	-0.39	-0.63	0.64	-1.2
Co-NP@NPC	0.4	-0.46	-0.62	0.57	-1
O*					
Co-SA@NPC	0.95	-0.58	-	-	-1.14
Co-NP@NPC	0.34	-0.79	-	-	-0.99
HO*					
Co-SA@NPC	0.91	-0.98	-	0.58	-1.27
Co-NP@NPC	0.33	-1.05	-	0.57	-1.15

Table S4. Comparison of electrochemical oxygen reduction reaction activity (onset, halfwave potential and Tafel slope), selectivity (electron transfer number, n) and stability of state-of-the-art non-precious group metal catalysts reported during the last five years.

Catalyst	E_{onset} /V	$E_{1/2}$ /V	Tafel mV/dec	n	Stability	*Reference*
Co-NP/Co-SA@NPC	0.96	0.87	54.5	3.8	97.5% 36000 s	*This Work*
CoTPP-pyrolyzed	0.88	0.82	60	3.1	-	*Sci Rep.* 2022,**12**, *8072*
CoPc@750	0.87	0.78	57	3.5-3.75	98.8% 5000 cycles	*Green Chem.* 2021, **23**, 3115
Co/CoN_x/NC	0.93	0.85	-	3.87	-18mV 5000 cycles	*J. Mater. Chem. A* 2022, **10**, 16920
Co_{40}SA/AC@NG	0.98	0.89	90	3.91-3.95	94.5% 90000 s	*Adv. Funct. Mater.* 2023, **33**, 2209726
Co_2/Fe-N@CHC	1.03	0.92	62	3.97-3.99	91.1% 100 h	*Adv. Mater.* 2021, **33**, 2104718
Co_3HITP_2	0.91	0.8	89	3.97	90% 36000 s	*Angew. Chem. Int. Ed.* 2020, **59**, *286*
CoO_x/CoN_y@CN_2, 700	0.9	0.83	61	3.9	96.1% 40 h	*Appl. Catal. B* 2020, **279**, 119407
Co-Ni-SAS/NC	0.88	0.76	--	~3.9	90% 57600 s	*Adv. Mater.* 2019, **31**, 1905622
Co@N-CNTF-2	0.91	0.81	-	3.96	92.3%	*J. Mater. Chem. A* 2019, **7**, 3664–3672
Co-SAs/N–C/rGO	1.01	0.84	-	~3.94	89.8% 2000 s	*J. Mater. Chem. A* 2023, **11**, 2291
Co-CNT/Ti_3C_2-60	-	0.84	63	3.9	90% 10000 s	*J. Mater. Chem. A* 2019, **7**, 1281
FeCo-N-HCN	0.98	0.86	52.1	3.96	~95% 35000 s	*Adv. Funct. Mater.* 2021, **31**, 2011289
FeCo–N–C	-	0.9	79.1	3.8-4.0	-4mV 5k cycle	*J. Mater. Chem. A* 2021, **9**, 13678–13687
Fe-ACSA@NC	1.03	0.9	78	~3.5	92% 43200 s	*Angew. Chem. Int. Ed.* 2022, **61**, e202116068
Fe- NCNT15R	0.92	0.76	118	3.92-3.82	Stable 2.5k cycles	*ACS Appl. Mater. Interfaces* 2020, **12**, 36026
Fe-N_4S_1	-	0.88	47.84	~4	90% 40000 s	*J. Mater. Chem. A* 2023, **11**, 11326–11333

Cu-Se Das	-	0.91	30.6	3.96	-16mV 10k cycles	*Angew. Chem. Int. Ed.* 2023, **62**, e202217719
Fe-SA/ PNC	1.04	0.92	68	3.99- 4.06	Stable 30k cycles	*Angew. Chem. Int. Ed.* 2023, **62**, e202307504
FeMnac/Mn-N_4C	1	0.9	87.4	3.97	99.1% 60000 s	*Angew. Chem. Int. Ed.* 2023, **62**, e202214988
CeO2/ $MnWO_4^{-2}$	-	0.83	-	3.1	-5mV 5000 cycles	*J Mater Sci. Mater. Electron.* 2022, **33**, 9538
MnPi-1.0	-	0.81	76	3.85- 3.91	89.3% 43200 s	*ChemNanoMat* 2022, **8**, e202200245
CuNCs– CoNCs/NPCF	0.97	0.85	42.7	3.95	-12mV 6000 cycles	*J. Mater. Chem. A* 2023, **11**, 4717–4728
H-S-Fe-NC	-	0.91	45.2	~4	97.7% 36000 s	*J. Mater. Chem. A* 2023, **11**, 16180
FeCu-SAC	-	0.93	53.6	3.93	85% 86400 s	*J. Mater. Chem. A* 2023, **11**, 6191–6197

References

S1. K. J. Msayib and N. B. McKeown, Inexpensive Polyphenylene Network Polymers with Enhanced Microporosity. *J. Mater. Chem. A* 2016, **4**, 10110–10113.

S2. A. D. Adler, F. R. Longo, J. D. Finarelli, J. Goldmacher, J. Assour and L. Korsakoff, A Simplified Synthesis for meso-Tetraphenylporphyrin. *J. Org. Chem.* 1967, **32**, 476.

S3. G. Kresse and J. Furthmüller, Efficiency of Ab Initio Total Energy Calculations for Metals and Semiconductors using a Plane Wave Basis Set. *Comput. Mater. Sci.* 1996, **6**, 15–50.

S4. G. Kresse and D. Joubert, From Ultrasoft Pseudopotentials to the Projector Augmented-Wave Method. *Phys. Rev. B: Condens. Matter Mater. Phys.* 1999, **59**, 1758.

S5. J. P. Perdew, K. Burke, M. Ernzerhof, Generalized Gradient Approximation Made Simple. *Phys. Rev. Lett.* 1996, **77**, 3865.

S6. A. H. Larsen, J. J. Mortensen, J. Blomqvist, I. E. Castelli, R. Christensen, M. Dułak, J. Friis, M. N. Groves. B. Hammer and C. Hargus, *J. Phys.: Condens. Matter* 2017, **29**, 273002.

S7. S. Grimme, J. Antony, S. Ehrlich and H. Krieg, A Consistent and Accurate Ab Initio Parametrization of Density Functional Dispersion Correction (DFT-D) for the 94 Elements Hydrogen-Plutonium. *J. Chem. Phys.* 2010, **132**, 154104.

S8. W. Tang, E. Sanville and G. Henkelman, A Grid-Based Bader Analysis Algorithm without Lattice Bias. *J. Phys.: Condens. Matter* 2009, **21**, 084204.

S9. V. Wang, N. Xu, J. C. Liu, G. Tang and W. T. Geng, VASPKIT: A User-Friendly Interface Facilitating High-Throughput Computing and Analysis Using VASP Code. *Comp. Phys. Commun.* 2021, **267**, 108033.